



# Influence of Cr<sup>3+</sup> substituted NiZnCo nano-ferrites: structural, magnetic and DC electrical resistivity properties

G. Vishnu Priya<sup>1</sup> · N. Murali<sup>2</sup> · M. K. Raju<sup>3</sup> · Bal Krishan<sup>4</sup> · D. Parajuli<sup>5</sup> · Praveen Choppara<sup>6</sup> · B. Chandra Sekhar<sup>7</sup> · Ritesh Verma<sup>8</sup> · Khalid Mujasam Batoo<sup>9</sup> · P. V. Lakshmi Narayana<sup>1</sup>

Received: 10 January 2022 / Accepted: 23 June 2022 / Published online: 11 July 2022  
© The Author(s), under exclusive licence to Springer-Verlag GmbH, DE part of Springer Nature 2022

## Abstract

This report synthesized the Cr<sup>3+</sup>-substituted NiZnCo ferrite nanoparticles using the sol–gel auto-combustion method. The X-ray diffraction (XRD) pattern revealed the formation of single-phase spinel cubic ferrite. The lattice constant is observed to increase from 8.34 Å to 8.47 Å for  $x=0.05$  and further decreases to 8.38 Å with the further increase in doping, whereas crystallite size decreases from 32.15 nm to 25.68 nm. Field Emission Scanning Electron Microscopy (FESEM) shows that grain size increases initially with Cr<sup>3+</sup> concentration, whereas for  $x=0.2$ , grain size decreases. Fourier Transform Infrared Spectroscopy (FTIR) shows the formation of peak  $\nu_1$  around 600 cm<sup>-1</sup> and  $\nu_2$  around 400 cm<sup>-1</sup>, confirming the formation of spinel structure. The reducing saturation magnetization from 68.49 emu/g to 51.64 emu/g with the addition of Cr<sup>3+</sup> ions shows a higher B–B interaction than A–B interaction. The DC resistivity increased with the increase in dopant concentration till  $x=0.1$ , and with further increase in doping concentration, the resistivity decreased.

**Keywords** NiZnCo ferrites · XRD · FESEM · FTIR · Magnetic properties

✉ N. Murali  
muraliphda@gmail.com

<sup>1</sup> Department of Nuclear Physics, Andhra University, Visakhapatnam, Andhra Pradesh 530003, India

<sup>2</sup> Department of Engineering Physics, AUCE (A), Andhra University, Visakhapatnam, India

<sup>3</sup> Department Physics, WISTM Engineering College, Pinagadi, Visakhapatnam, Andhra Pradesh, India

<sup>4</sup> Department of Chemistry, Bahra University, Wagnaghat, Solan, Himachal Pradesh, India

<sup>5</sup> Research Center for Applied Science and Technology, Tribhuvan University, KTM, Kirtipur, Nepal

<sup>6</sup> Department of Chemistry, P. R. Government College (A), Kakinada, Andhra Pradesh 533001, India

<sup>7</sup> Vignani's Institute of Engineering for Women, Visakhapatnam 530046, India

<sup>8</sup> School of Physics and Materials Science, Shoolini University, Solan, Himachal Pradesh 173212, India

<sup>9</sup> College of Science, King Saud University, P.O. Box-2455, Riyadh 11451, Saudi Arabia

## 1 Introduction

In most practical applications, ferrites of mixed variety have been used to make various electronic devices [1, 2]. The ferrites with (Nickel and Zinc) Ni–Zn combination are more advanced than the simple ones with Ni, Zn, Cu, Mg, etc. due to their higher frequency following higher permeability [3, 4] along with good electrical resistivity, mechanical hardness, and sufficiently low costs [5] enabling these ferrites suitable for different microwave absorbers, electronics devices, and transformer cores [6–12].

For most ferrite groups, the synthesis methods, chemical composition, and sintering temperature decide Ni–Zn ferrites' properties by replacing the cation site either in tetrahedral or octahedral coordination [13]. The sol–gel, co-precipitation, and hydrothermal processes are the most commonly used methods for synthesizing Ceramic materials [14–16]. The ferrites' magnetic, electrical, and dielectric properties depend on the preparation methods [17] and the cation's occupancy in the two interstitial sites. The occupancy of Ni<sup>2+</sup> in the octahedral site gives rise to Ni-ferrites' inverse spinel structure, whereas Zn<sup>2+</sup> in the tetrahedral place give Zn ferrite as normal ferrite [18]. In Ni–Zn ferrite materials, site preference of cations at the usual sites would be

inevitable and different properties that will be exploited are the results of such material [19]. Among them, Ni–Zn ferrite is highly stable at a higher frequency. Surface Mounting Devices (SMDs) mostly use (Nickel Zinc Cobalt) NiZnCo ferrites [20–22]. As a result, they are utilized in cellular phones, video cameras, notebook computers, electromagnetic interference (EMI) shielding, personal wireless communication systems, etc. their properties can be changed by varying the concentration of  $\text{Co}^{2+}$  and are more applicable in inductive devices like transformers [23, 24]. The ferrites prepared at low temperatures are used in multilayer power inductors and transformers [25].

It has been observed that the  $\text{Cr}^{3+}$  decreases the saturation magnetization and coercivity and increases the superparamagnetic behavior [26]. In addition, the substitution of  $\text{Cr}^{3+}$  ions as a dopant significantly reduces the dielectric loss, dielectric constant, and electrical conductivity and increases the resistivity [27]. Thus, the decrease in dielectric constant and dielectric loss can significantly improve a material's high-frequency applications. Hence, the substitution of  $\text{Cr}^{3+}$ -doped NiZnCo ferrite nanoparticles are prepared that could be used for high-frequency applications. In this paper,  $\text{Cr}^{3+}$  substitution on NiZnCo ferrite nanoparticles at the  $\text{Fe}^{3+}$  site is studied, and their structural, dc electrical resistivity and magnetic properties were investigated.

## 2 Experimental methods

The spinel structured  $\text{Ni}_{0.40}\text{Zn}_{0.35}\text{Co}_{0.25}\text{Fe}_{2-x}\text{Cr}_x\text{O}_4$  ( $x = 0.00, 0.05, 0.10, 0.15, 0.20$ ) ferrite nanoparticles are synthesized using the sol–gel auto-combustion method. The chemicals used are the Nitrates of Zinc [ $\text{Zn}(\text{NO}_3)_2 \cdot 0.6(\text{H}_2\text{O})$ ], Nickel [ $\text{Ni}(\text{NO}_3)_2 \cdot 0.6(\text{H}_2\text{O})$ ], Cobalt [ $\text{Co}(\text{NO}_3)_2 \cdot 0.6(\text{H}_2\text{O})$ ], Chromium [ $\text{Cr}(\text{NO}_3)_3 \cdot 0.9(\text{H}_2\text{O})$ ], Ferric [ $\text{Fe}(\text{NO}_3)_3 \cdot 0.9(\text{H}_2\text{O})$ ] and the Citric acid monohydrate ( $\text{C}_6\text{H}_8\text{O}_7 \cdot \text{H}_2\text{O}$ ) and Ammonium hydroxide ( $\text{NH}_3\text{H}_2\text{O}$ ) are used as precursor materials. All chemicals used are purchased from Sigma Aldrich and are of high purity. Here, citric acid ( $\text{C}_6\text{H}_8\text{O}_7 \cdot \text{H}_2\text{O}$ ) is used as the chelating agent. The ratio of citric acid to the metal ions is maintained at 1:1. First, all-metal nitrated are dissolved in deionized water, and the citric acid solution is added to the metal nitrate solution. With constant stirring, ammonium hydroxide is added slowly to this solution to control the pH value at 7. The stirring is continued with a magnetic stirrer, and the temperature is maintained at 80 °C until a gel is formed. The precursor gel is dried overnight in an oven at 150 °C to remove moisture traces to obtain the dry material. The obtained powder is calcinated for 4 h at 800 °C at the rate of 5 °C per minute. Thus, the ferrite powder, which is grounded finely with the help of agate mortar and pestle, is then pressed into a pellet with 5 tons of hydraulic pressure. The pellets were finally sintered at 900 °C for 2 h.

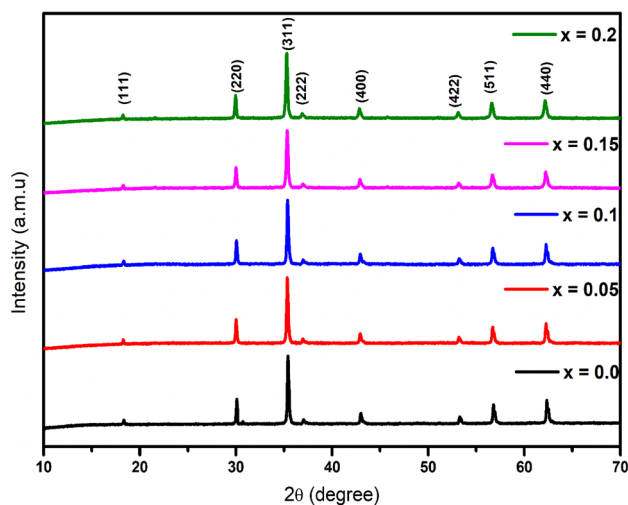
The Rigaku X-ray Diffractometer (TESCEN) is used for the structural analysis of all samples. The morphology was observed using Field Emission Scanning Electron Microscope (MIRA II LMH). FTIR analysis was done using the FTIR instrument of Shimadzu FTIR-8900 for the functional group analysis. To know the magnetic properties, EZ VSM is used at room temperature. A two-probe DC resistivity apparatus (TPX-200C) is used to see the resistivity of all the samples. Bulk electrical resistivity is measured using the two-probe method, commonly known as the uniaxial method. The specimen is put between two electrodes with wet sponge contacts, and a DC electric current is administered to detect the resulting potential decrease.

## 3 Results and discussion

### 3.1 XRD studies

The XRD pattern was recorded for all the samples in the range of 10°–80° with 2° increments in step size to identify the phase formation and other structural parameters. Figure 1 represents the XRD pattern along with (hkl) planes of as-synthesized nano-ferrite having the following composition  $\text{Ni}_{0.40}\text{Zn}_{0.35}\text{Co}_{0.25}\text{Fe}_{2-x}\text{Cr}_x\text{O}_4$  ( $x = 0.00, 0.05, 0.10, 0.15, 0.20$ ). Figure 1 shows that clear and smooth intensity peaks around (220), (311), (222), (400), (420), (511), and (440) are observed, indicating the cubic spinel with a single-phase having Fd3m space group with JCPDS card numbers 22-1086 [28].

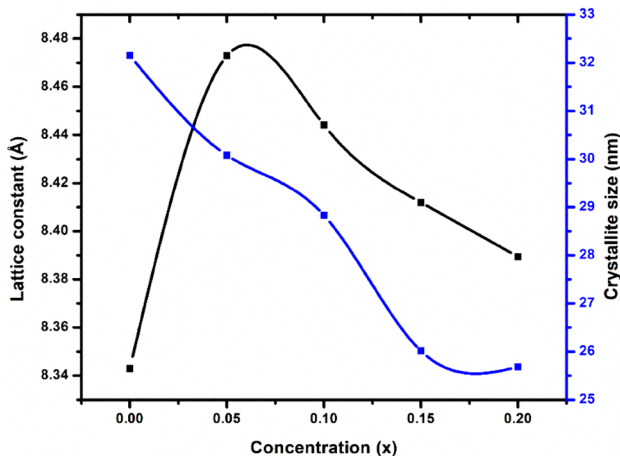
The lattice constant 'a' is determined with the following relation and presented in Table 1 [19].



**Fig. 1** X-ray powder diffraction for  $\text{Ni}_{0.40}\text{Zn}_{0.35}\text{Co}_{0.25}\text{Fe}_{2-x}\text{Cr}_x\text{O}_4$  ferrite NPs

**Table 1** Lattice parameters of Ni<sub>0.40</sub>Zn<sub>0.35</sub>Co<sub>0.25</sub>Fe<sub>2-x</sub>Cr<sub>x</sub>O<sub>4</sub> ferrite NPs

Compound	a (Å)	Cell volume (Å) <sup>3</sup>	Crystallite (nm)	Space group	Grain size (nm)
0.0	8.343	611.493	32.15	<i>Fd-3 m</i>	42
0.05	8.472	608.272	30.08	<i>Fd-3 m</i>	114
0.1	8.444	602.094	28.83	<i>Fd-3 m</i>	185
0.15	8.411	595.234	26.01	<i>Fd-3 m</i>	258
0.2	8.389	590.456	25.68	<i>Fd-3 m</i>	227

**Fig. 2** Variation of lattice constant and crystallite size of Cr<sup>3+</sup>-substituted NiZnCo nano-ferrites

$$a = d_{hkl} \sqrt{h^2 + k^2 + l^2}, \quad (1)$$

where  $d_{hkl}$  is the interplanar spacing of (hkl) planes and is calculated by Bragg's law. Here, the highest intensity is obtained for the (311) peak. The highest peak (311 planes) is used to determine the crystallite size using Scherer's Formula [29, 30]:

$$t = \frac{0.89\lambda}{\beta \cos\theta}, \quad (2)$$

where  $t$  is the average crystallite size in (nm),  $\beta$  the FWHM with the X-ray of wavelength  $\lambda$  having diffracting angle  $2\theta$ . On average, the calculated average size of NPs was in the range of 32.15–25.68 nm, whereas the lattice constants are in the range of 8.343–8.47 Å. The Cr<sup>3+</sup> doping increases the lattice parameters to 8.47 Å for  $x=0.05$ . With further doping, the lattice parameters are observed to decrease slightly due to Vegard's law [31, 32], as shown in Fig. 2. The increase in lattice parameter for  $x=0.05$  might be because of the substitution of Cr<sup>3+</sup> ions at Co<sup>3+</sup> ions. In addition, the Substitution of Cr<sup>3+</sup> at the Fe<sup>3+</sup> cation can also cause the ion exchange of Fe ions at the A and B sites of the spinel ferrite. The decrease in lattice parameter with the rise of Cr<sup>3+</sup> is reasoned out as a replacement of lower

ionic radius Fe<sup>3+</sup> (0.67 Å) with higher ionic radius Cr<sup>3+</sup> (0.62 Å) [33].

### 3.2 FESEM studies

The FESEM gives the surface morphology and texture of Ni<sub>0.40</sub>Zn<sub>0.35</sub>Co<sub>0.25</sub>Fe<sub>2-x</sub>Cr<sub>x</sub>O<sub>4</sub> ( $x=0.00, 0.05, 0.10, 0.15, 0.20$ ) ferrite nanoparticles. The micrographs show the nanograins of sizes ranging from 40 to 258 nm, as shown in Fig. 3. It is observed that, with the Cr<sup>3+</sup> ions doping, the grain size increases till  $x=0.15$  and then decreases for further doping. At the same time, the agglomeration is observed to increase with Cr<sup>3+</sup> doping, which is due to its accumulation at the surface of the samples. In addition, the crystallinity is observed to increase with the increase in doping concentration.

Furthermore, features such as grain size, porosity, and crystallinity are modified significantly, and these parameters are responsible for the electrical and magnetic properties [34]. The micrographs also observed that grains are irregular in shape with random orientations.

### 3.3 FTIR studies

The bonding nature and the cation site occupation is studied by employing room temperature FT-IR measurements for Ni<sub>0.40</sub>Zn<sub>0.35</sub>Co<sub>0.25</sub>Fe<sub>2-x</sub>Cr<sub>x</sub>O<sub>4</sub> ( $x=0.00, 0.05, 0.10, 0.15, 0.20$ ) samples. As observed in Fig. 4, the two major absorption bands are observed that confirmed the formation of spinel structure [35]. The band at the lower frequency ( $\nu_2$ ) around 400–410 cm<sup>-1</sup> represents the octahedral metal cation-oxygen bond vibrations and stretching. The higher frequency band ( $\nu_1$ ) around 580–600 cm<sup>-1</sup> represents the tetrahedral site metal-oxygen stretching and vibrations (Table 2) [36]. Though there are other absorption peaks, the dominants are the so mentioned ones that signify the spinel ferrite structures. The samples' tetrahedral and octahedral site vibrations in NiZnCo ferrite are due to the Zn–O–Co and Ni–O vibrations, respectively.

Moreover, the increase in vibrational mode is observed from 580.41 to 599.39 cm<sup>-1</sup> for the tetrahedral site. However, the absorption peak for the tetrahedral site might have shifted toward the lower side of the observed wavenumber, i.e. < 400 cm<sup>-1</sup>. Due to this, we cannot describe the

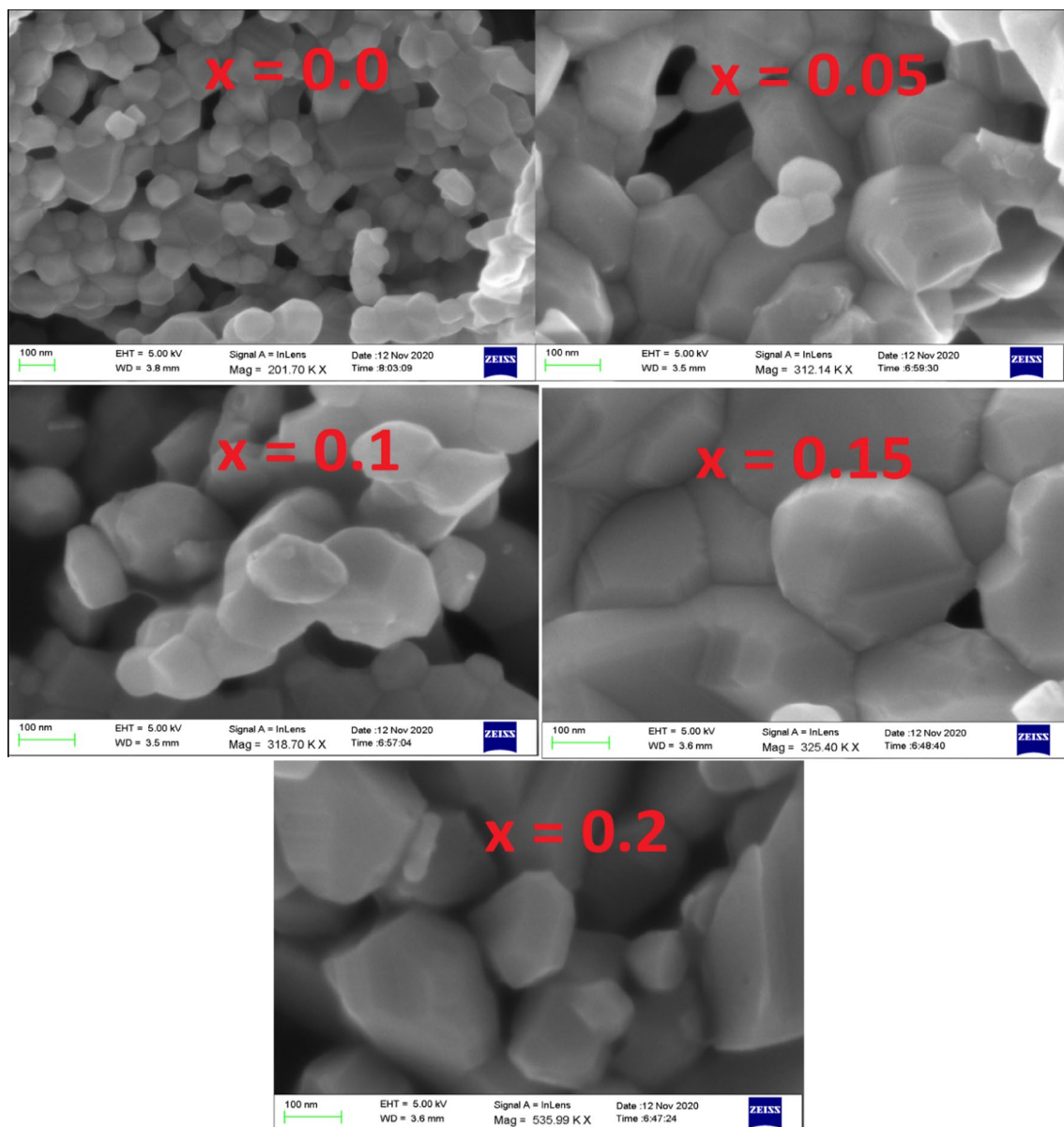


**Fig. 3** FESEM images for  $\text{Ni}_{0.40}\text{Zn}_{0.35}\text{Co}_{0.25}\text{Fe}_{2-x}\text{Cr}_x\text{O}_4$  ferrite NPs

tetrahedral site position. As obtained from XRD analysis, the shifting of octahedral and tetrahedral vibrational mode corresponds to the change in lattice parameters with the increase in doping concentration.

### 3.3.1 VSM studies

The magnetic parameters of  $\text{Ni}_{0.40}\text{Zn}_{0.35}\text{Co}_{0.25}\text{Fe}_{2-x}\text{Cr}_x\text{O}_4$  ( $x = 0.00, 0.05, 0.10, 0.15, 0.20$ ) samples are recorded at room temperature. The nanostructures significantly influence the magnetic nature by determining the shape of magnetic domains [29]. As shown in Fig. 5, similar hysteresis curves are observed for all the samples. Magnetic

parameters such as magnetic saturation ( $M_s$ ) and a coercive field ( $H_c$ ) are obtained from these curves with the variation of  $\text{Cr}^{3+}$  content. It is observed that the value  $M_s$  first increased till  $x = 0.1$  and then decreased with an increase in  $\text{Cr}^{3+}$  ions. The initial increase in  $M_s$  value is due to the substitution of  $\text{Cr}^{3+}$  ions at  $\text{Co}^{3+}$  ions, leading to the increase in A–B interaction. In addition, the substitution of  $\text{Cr}^{3+}$  at the  $\text{Fe}^{3+}$  site can also cause the ion exchange of Fe ions at the A and B sites of the spinel ferrite, again contributing to the increase in A–B interaction. The decrease in  $M_s$  value is due to the decrease in Fe ion exchange, which decreases A–B interaction strength. This leads to the increase in B–B interaction in the present system [37].

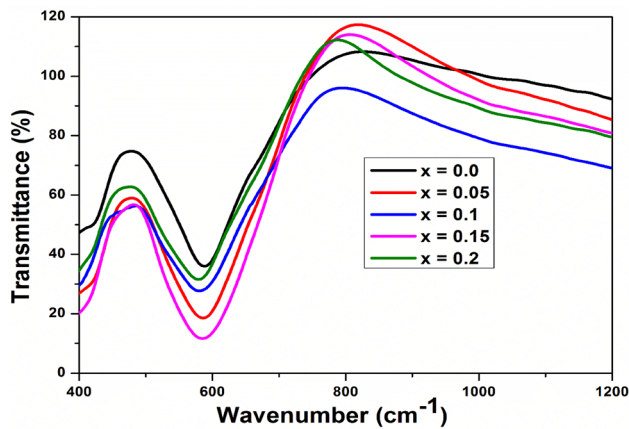


**Fig. 4** Infrared spectra of Ni<sub>0.40</sub>Zn<sub>0.35</sub>Co<sub>0.25</sub>Fe<sub>2-x</sub>Cr<sub>x</sub>O<sub>4</sub> ferrite NPs

**Table 2** Octahedral ( $\nu_2$ ) and tetrahedral ( $\nu_1$ ) absorption bands of Ni<sub>0.40</sub>Zn<sub>0.35</sub>Co<sub>0.25</sub>Fe<sub>2-x</sub>Cr<sub>x</sub>O<sub>4</sub> ferrite NPs

Compounds	Tetrahedral absorption bands $\nu_1$ (cm <sup>-1</sup> )
0.0	580.41
0.05	583.25
0.1	586.07
0.15	590.23
0.2	599.39

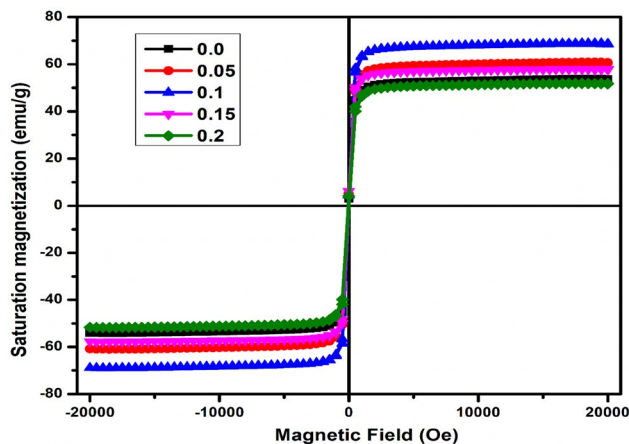


**Fig. 5** Hysteresis curve of Ni<sub>0.40</sub>Zn<sub>0.35</sub>Co<sub>0.25</sub>Fe<sub>2-x</sub>Cr<sub>x</sub>O<sub>4</sub> NPs at room temperature

It can be observed from Fig. 6 that the maximum value of Ms is 68.49 emu/g for x = 0.10.

We also calculated the magnetic moment per formula unit using the formula presented in Table 3 [38]:

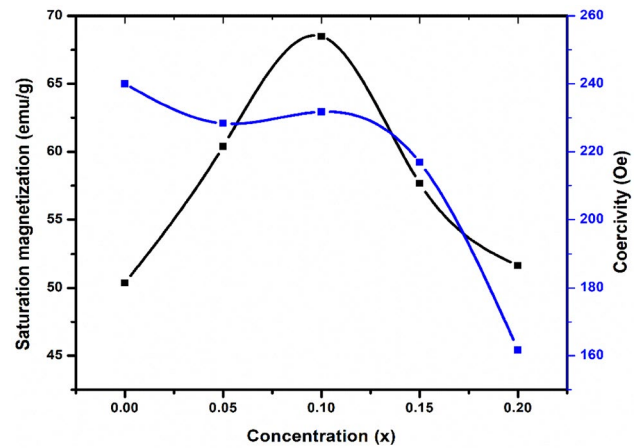


**Fig. 6** Variation of saturation magnetization and coercivity of Ni<sub>0.40</sub>Zn<sub>0.35</sub>Co<sub>0.25</sub>Fe<sub>2-x</sub>Cr<sub>x</sub>O<sub>4</sub> NPs

**Table 3** Saturation magnetization (Ms), remanent magnetization (Mr) and coercivity (Hc) of Ni<sub>0.40</sub>Zn<sub>0.35</sub>Co<sub>0.25</sub>Fe<sub>2-x</sub>Cr<sub>x</sub>O<sub>4</sub> ferrite NPs

Compounds	Ms (emu/g)	Hc (Oe)	$\mu_B$
0.00	53.37	240	2.26
0.05	60.46	228.34	2.56
0.10	68.49	231.75	2.89
0.15	57.67	216.86	2.43
0.20	51.64	161.67	2.18

$$\mu_B = \frac{M \times M_s}{5585} \quad (3)$$

M is the molecular weight of a particular composition, and M<sub>s</sub> is the saturation magnetization (emu/g). The calculated results for the present samples show that the value of  $\mu_B$  Initially increases till x = 0.1 and then decreases further with the increase in Cr<sup>3+</sup> ions concentration. This variation can be related to the variation of saturation magnetization value.

### 3.4 DC electrical resistivity

Initially, the DC resistivity of Ni<sub>0.40</sub>Zn<sub>0.35</sub>Co<sub>0.25</sub>Fe<sub>2-x</sub>Cr<sub>x</sub>O<sub>4</sub> (x = 0.00, 0.05, 0.10, 0.15, 0.20) shows a plateau-like behavior with the increase in temperature. In contrast, the resistivity decreases significantly with further temperature increases, as shown in Fig. 7. The log  $\rho$  vs. 1000/T plot in the range 35–200 °C shows the negative temperature coefficient with resistance. This shows that all samples behave like typical semiconductors. It is also observed that the Cr<sup>3+</sup> doping resistivity shows almost similar variation. The plots have straight lines whose

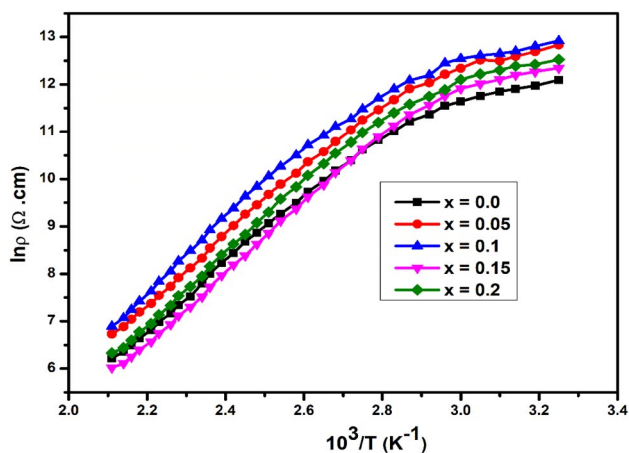


**Fig. 7** Temperature dependence of DC resistivity of Ni<sub>0.4</sub>Zn<sub>0.35</sub>Co<sub>0.25</sub>Fe<sub>2-x</sub>Cr<sub>x</sub>O<sub>4</sub> ferrite nanoparticles

slopes are used for the calculation of activation energies of the charge carries following hopping mechanism [39]:

$$\sigma = \sigma_0 \cdot \exp\left(-\frac{E_a}{k_B T}\right), \tag{4}$$

where  $\Delta E$  is the activation energy,  $K$  is the Boltzmann constant. The fitted curves are presented in Fig. 8. The calculated values of activation energies of the ferrite nanoparticles are shown in Fig. 9.

Verwey and de Boer explained the hopping mechanism according to which the jumping of electrons occurs between the different valence states of the same elements distributed over various sites [40, 41]. The generation of Fe<sup>2+</sup> ions in the sintering process and their existence in

the two interstitial sites give rise to Fe<sup>2+</sup> ⇌ Fe<sup>3+</sup> hopping mechanism. There is also another hopping Cr<sup>2+</sup> ⇌ Cr<sup>3+</sup> and similarly for Ni, Co, Zn, and Cr cations in octahedral sites, which is responsible for the uneven variation of DC resistivity at higher doping concentrations. [42].

The mobility of the electron depends upon their drift and diffusion caused by the temperature effect and hence affecting the resistivity. The log σ vs. 1000/T plot gives the activation energies in the range of 0.008–0.0114 eV. The activation energy reported earlier for Fe<sup>2+</sup> ⇌ Fe<sup>3+</sup> was just 0.21 eV [43], indicating this present work's effectiveness. Now the decrease in activation energy with respect to the previously reported literature is due to the doping of Cr<sup>3+</sup> ions. Furthermore, the irregular variation in activation energy is due to the substitution of Cr<sup>3+</sup> at the Fe<sup>3+</sup> site can also cause the ion exchange of Fe ions at the A and B sites of the spinel ferrite. All these phenomena indicate the compositional dependency of dc resistivity [44].

### 4 Conclusions

The sol–gel auto-combustion method is used for the preparation of the samples with Ni<sub>0.40</sub>Zn<sub>0.35</sub>Co<sub>0.25</sub>Fe<sub>2-x</sub>Cr<sub>x</sub>O<sub>4</sub> (x = 0.00, 0.05, 0.10, 0.15, 0.20) nano-ferrites. They are observed to show a spinel structure without any impurity phase. The lattice parameters are observed to decrease with an increase in Cr<sup>3+</sup> concentration. The grains are observed to have irregular shape and orientation, and the grain size first increased to x = 0.1 and then decreased with Cr<sup>3+</sup> content. The saturation magnetization first increases up to x = 0.1 and then decreases with the doping while the coercive force decreases gradually with increasing the concentration. The two-probe method found the semiconducting nature in the DC electrical resistivity test.

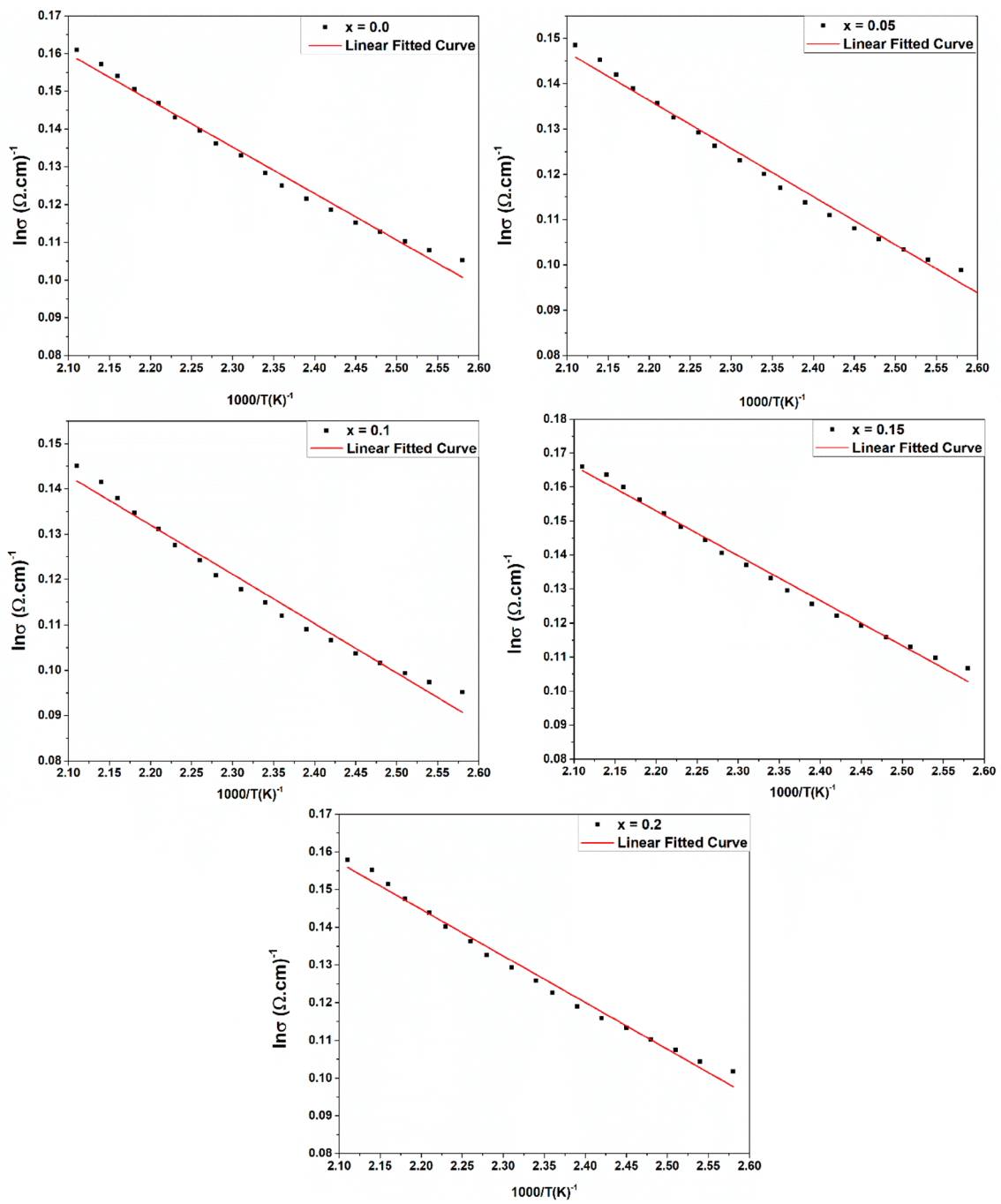
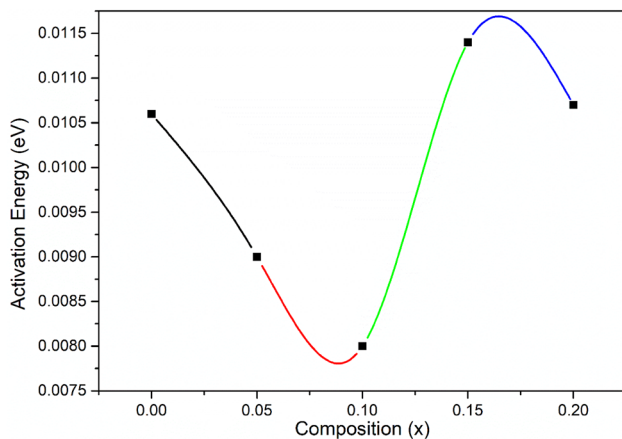


Fig. 8 Activation Energy Fitting graphs of Ni<sub>0.4</sub>Zn<sub>0.35</sub>Co<sub>0.25</sub>Fe<sub>2-x</sub>Cr<sub>x</sub>O<sub>4</sub> ferrite nanoparticles



**Fig. 9** Activation energies of the  $\text{Ni}_{0.40}\text{Zn}_{0.35}\text{Co}_{0.25}\text{Fe}_{2-x}\text{Cr}_x\text{O}_4$  ferrite nanoparticle

**Acknowledgements** This research received no external funding.

## Declarations

**Conflict of interest** There are no conflicts to declare.

## References

- U. Chandan, H.C. Verma, *J. Appl. Phys.* **95**(10), 5746–5751 (2004)
- M. Abdullah Dar, J. Shah, W.A. Siddiqui, R.K. Kotnala, *Appl. Nanosci.* **4**, 675–682 (2014)
- M. Sorescu, L. Diamandescu, R. Peelamedu, R. Roy, P. Yadoji, *J. Magn. Magn. Mater.* **279**, 195–201 (2004)
- N. Murali, S.J. Margarete, G.P. Kumar, B. Sailaja, S.Y. Mulushoa, P. Himakar, B.K. Babu, V. Veeraiah, *Physica B* **522**, 1–6 (2017)
- T.W. Mammo, N. Murali, Y.M. Sileshi, T. Arunamani, *Physica B* **523**, 24–30 (2017)
- A. Ramakrishna, N. Murali, T.W. Mammo, K. Samatha, V. Veeraiah, *Physica-B* **534**, 134–140 (2018)
- K.R. Krishna, K.V. Kumar, C. Ravindernathgupta, D. Ravinder, *Adv. Mater. Phys. Chem.* **2**, 149–154 (2012)
- D. Parajuli, K. Samatha, *J. Phys. Sci.* **18**, 128–133 (2020). (BIBECHANA)
- D. Parajuli, K. Samatha, *J. Phys. Sci.* **18**, 80–86 (2021). (BIBECHANA)
- D. Parajuli, V. Raghavendra, B. Suryanarayana, P.A. Rao, N. Murali, P.V.S.K.P. Varma, R.G. Prasad, Y. Ramakrishna, K. Chandramouli, *Results Phys.* **23**, 103947 (2021)
- D. Parajuli, N. Murali, K. Samatha, *JNPS* **7**, 24–32 (2021)
- D. Parajuli, P. Tadesse, N. Murali, K. Samatha, *Appl. Phys. A* **128**, 58 (2022)
- O.F. Caltun, L. Spinu, A. Stancu, *IEEE Trans. Magn.* **37**, 2353–2355 (2001)
- K. Chandramouli, B. Suryanarayana, P.V.S.K.P. Varma, V. Raghavendra, K.A. Emmanuel, P. Tadesse, N. Murali, T.W. Mammo, D. Parajuli, *Results Phys.* **24**, 104117 (2021)
- R. Jasrotia, J. Prakash, G. Kumar, R. Verma, S. Kumari, S. Kumar, V.P. Singh, A.K. Nadda, S. Kalia, *Chemosphere* **294**, 133706 (2022)
- R. Verma, A.N. Chauhan, K.M. Batoo, R. Kumar, M. Hadi, E.H. Raslan, *Ceram. Int.* **47**, 3680–3691 (2021)
- P.L. Leng, M.G. Naseri, E. Saion, A.H. Shaari, M.A. Kamaruddin, *Adv. Nanoparticles* **2**, 378–383 (2013)
- M.R. Patil, M.K. Rendale, S.N. Mathad, R.B. Pujar, *Inorg. Nano-Met Chem.* **47**, 1145–1149 (2017)
- R. Kumar, R.R. Singh, P.B. Barman, *Int. J. Sci. Eng. Res.* **5**, 12–20 (2014)
- D.R.S.G. Swamy, M.C. Varma, K.S. Rao, K.H. Rao, *Indian J. Res. Pharm. Biotechnol.* 59–67 (2014)
- M. Ashar, A. Munir, M. Anis-ur-Rehman, A. Maqsood, *Mater. Res. Bull.* **79**, 14–21 (2016)
- A.M. El-Sayed, *Ceram. Int.* **28**, 651–655 (2002)
- A. Globus, H. Pascard, V.C. Agan, *J. Phys. Colloq.* **38**, 161 (1977)
- K.M. Batoo, M. Hadi, R. Verma, A. Chauhan, R. Kumar, M. Singh, O.M. Aldossary, *Ceram. Int.* **48**, 3328–3343 (2022)
- S.K. Nath, M.M. Rahman, S.S. Sikder, M.A. Hakim, *ARPN J. Sci. Technol.* **3**, 106–111 (2013)
- Y. Koseoglu, *Ceram. Int.* **41**, 6417–6425 (2015)
- S. Nasir, M. Anis-Ur-Rehman, M.A. Malik, *Phys. Scr.* **83**, 025602 (2011)
- E.W. Gorter, *Philips Res. Rep.* **9**, 321 (1954)
- R.C. Kambale, P.A. Shaikh, C.H. Bhosale, K.Y. Rajpure, Y.D. Kolekar, *Smart Mater. Struct.* **18**, 115028 (2009)
- M. Shandilya, R. Verma, *J. Magn. Magn. Mater.* **527**, 167782 (2021)
- M. Anis-ur-Rehman, M.A. Malik, K. Khan, A. Maqsood, *J. Nano Res.* **14**, 1–9 (2011)
- K.M. Batoo, R. Verma, A. Chauhan, R. Kumar, M. Hadi, O.M. Aldossary, Y. Al-Douri, *J. Alloy. Compd.* **883**, 160836 (2021)
- E.J.W. Verwey, J.H. de Boer, *Rec. Trav. Chim.* **55**, 53 (1936)
- M. Rosenberg, M. Velicescu, *J. Phys. Soc. Jpn.* **28**, 264 (1970)
- P.A. Rao, V. Raghavendra, B. Suryanarayana, T. Paulos, N. Murali, P.P. Varma, R.G. Prasad, Y. Ramakrishna, K. Chandramouli, *Results Phys.* **19**, 103487 (2020)
- P. Himakar, K. Jayadev, D. Parajuli, N. Murali, P. Tadesse, S.Y. Mulushoa, T.W. Mammo, B.K. Babu, V. Veeraiah, K. Samatha, *Appl. Phys.* **127**(5), 1–10 (2021)
- T.W. Mammo, C.V. Kumari, S.J. Margarete, A. Ramakrishna, R. Vemuri, Y.S. Rao, K.V. Prasad, Y. Ramakrishna, N. Murali, *Physica B* **581**, 411769 (2020)
- M.A. Anis-ur-Rehman, K.K. Malik, A. Maqsood, *J. Nano Res.* **14**, 1–9 (2011)
- A. Ramakrishna, N. Murali, T.W. Mammo, K. Samatha, V. Veeraiah, *Physica B* **534**, 134–140 (2018)
- G. Raju, N. Murali, M.S.N.A. Prasad, B. Suresh, D.A. Babu, M.G. Kiran, A. Ramakrishna, M.T. Wegayehu, B.K. Babu, *Mater. Sci. Energy Technol.* **2**, 78–82 (2019)
- S.J. Mercy, N. Murali, A. Ramakrishna, Y. Ramakrishna, V. Veeraiah, K. Samatha, *Appl. Phys. A* **126**, 1–13 (2020)
- A. Ramakrishna, N. Murali, S.J. Margarete, K. Samatha, V. Veeraiah, *Physica B* **530**, 251–257 (2018)
- K. Ramanjaneyulu, B. Suryanarayana, V. Raghavendra, N. Murali, D. Parajuli, K. Chandramouli, *Solid State Technol.* **64**(2), 7192–7200 (2021)
- J.Z. Msomi, T. Moyo, T.B. Doyle, *J. Magn. Magn. Mater.* **310**(2), 2534–2536 (2007)

**Publisher's Note** Springer Nature remains neutral with regard to jurisdictional claims in published maps and institutional affiliations.